



Structure and Infrastructure Engineering

Maintenance, Management, Life-Cycle Design and Performance

ISSN: (Print) (Online) Journal homepage: <https://www.tandfonline.com/loi/nsie20>

Finite element based study on aerostatic post-buckling and multi-stability of long-span bridges

Lin Zhao, Teng Ma, Wei Cui & Yaojun Ge

To cite this article: Lin Zhao, Teng Ma, Wei Cui & Yaojun Ge (2023): Finite element based study on aerostatic post-buckling and multi-stability of long-span bridges, *Structure and Infrastructure Engineering*, DOI: [10.1080/15732479.2022.2164596](https://doi.org/10.1080/15732479.2022.2164596)

To link to this article: <https://doi.org/10.1080/15732479.2022.2164596>



Published online: 09 Jan 2023.



Submit your article to this journal



Article views: 17



View related articles



View Crossmark data



Finite element based study on aerostatic post-buckling and multi-stability of long-span bridges

Lin Zhao^{a,b,c}, Teng Ma^a, Wei Cui^{a,b,c} and Yaojun Ge^{a,b,c}

^aState Key Lab of Disaster Reduction in Civil Engineering, Tongji University, Shanghai, China; ^bDepartment of Bridge Engineering, College of Civil Engineering, Tongji University, Shanghai, China; ^cKey Laboratory of Transport Industry of Bridge Wind Resistance Technologies, Tongji University, Shanghai, China

ABSTRACT

Aerostatic instability is one of two vital instabilities of wind resistance design for long-span bridges. Traditionally, the aerostatic instability considering aerodynamic and structural nonlinearity is evaluated through finite element methods employing the Newton-Raphson algorithm. However, the Newton-Raphson algorithm cannot track the structural equilibrium path after the first critical wind speeds (zero stiffness point) and the potential post-buckling multi-stability. This study proposes to use the arc-length method to calculate the aerostatic structural deformation for increasing wind speeds iteratively. Arc-length can track the equilibrium force-deformation curve even after the initial critical wind speeds. This study finds out that when the pitch moment curve of the bridge deck has a "turning point" at a large angle of attack, there is possibly more than one equilibrium point (multi-stability) for the same wind speeds. Correspondingly, the bridge deck deformation shape and cable and hangers' internal force along span direction change dramatically at the same wind speed due to aerostatic multi-stability. In the last part of this study, the bridge structure under a turbulent wind field can buckle at a lower wind speed than a smooth wind field because the material yields are caused by large instantaneous deformation.

ARTICLE HISTORY

Received 10 May 2022
Revised 24 October 2022
Accepted 15 November 2022

KEYWORDS

Bridge failure; bridges; bridges; finite element method; long-span; structural stability; suspension; wind forces; wind loading; aerodynamics

1. Introduction

For flexible long-span bridges, there are two typical aerodynamic instabilities: aeroelastic flutter and aerostatic instability (Yang, Zhou, Ge, Mohotti, & Mendis, 2015). Flutter occurs when the periodically moving body in a fluid flow exhibits negative damping caused by positive feedback between bridge deck displacement and moving dependent aeroelastic force. Aerostatic instability, also known as torsional divergence, is caused by vanished torsional stiffness. On one side, the aerodynamic pitch moment increases the wind flow angle of attack (AoA) on the bridge deck, increasing the aerodynamic forces. Also, on the other side, the deck torsion deforms the cable-hanger-deck system to decrease the structural stiffness due to geometry nonlinearity. In the beginning, aerostatic stability is studied as the torsional divergence of flight wing in the aeronautic engineering field, which was defined by a critical wind speed at which the torsion caused negative aerodynamic stiffness to surpass structural stiffness, and structural torsion will increase unlimitedly (Bisplinghoff & Ashley, 2013).

At first, the critical wind speed can be calculated assuming that both pitch moment and structural restoring force increase linearly with torsional deformation. For long-span bridges, based on the same linearity assumption, the critical wind speeds can be derived from structural stiffness and aerodynamic pitch moments coefficients (Simiu & Yeo,

2019). In wind tunnel test of full-bridge models of long-span bridges, flutter usually occurs before torsional divergence (Simiu & Scanlan, 1996), but for some specific bridges, torsional divergence occurred under static wind loads (Hirai, Okauchi, Ito, & Miyata, 1967). Therefore, in modern engineering practice, the flutter and aerostatic instability are usually analyzed separately. Specifically, the evaluation of aerostatic instability ignores the dynamic and aeroelastic forces (Boonyapinyo, Lauhathanon, & Lukkunaprasit, 2006; Simiu & Scanlan, 1996) on structures and vice versa. Because it is difficult to conduct the repeatable the aerostatic instability experiment in wind tunnel, most research uses a numerical or analytical method to study this problem.

However, the linearity assumption usually is unsuitable for long-span bridges because of geometry nonlinearity, aerodynamic nonlinearity, and even material strength nonlinearity. Therefore, the finite element method (FEM) was employed to investigate the wind-induced nonlinear lateral-torsional buckling of cable-stayed bridges through combining eigenvalue analysis and updated bound algorithms (Boonyapinyo, Yamada, & Miyata, 1994). Later, the material strength nonlinearity was also considered in the lateral-torsional buckling analysis for suspension bridges (Boonyapinyo et al., 2006). At the same time, a two-level nested iteration method was developed based on nonlinear

FEM to analyze the aerostatic stability for suspension bridge (Cheng, Jiang, Xiao, & Xiang, 2002b) and cable-stayed bridge (Cheng, Jiang, Xiao, & Xiang, 2002a), and software was developed for general aerostatic stability analysis for long-span bridge (Cheng, Xiao, Xiang, & Jiang, 2003). Besides torsional divergence, it was also found out that the pretension vanishes are another criterion for long-span bridge lateral-torsion buckling (Zhang, Ge, & Chen, 2015). The effect of turbulence-induced vibration was also investigated that it could decrease the aerostatic stability of suspension bridge (Zhang, Chen, Hua, Li, & Ge, 2010).

Besides numerical simulation methods, analytical methods are also another essential tool for aerodynamic-induced torsional divergence. Classical analyses of torsional divergence, based on the linear assumption of aerodynamic force and structural stiffness, can be solved by a Sturm-Liouville eigenvalue problem (Bisplinghoff & Ashley, 2013). Other analytical methods considering geometrical and aerodynamic nonlinearity have also been developed for general beam (Dimentberg, 1999) and flight wings (Dunn & Dugundji, 1992) using in the field of aeronautics engineering. Long-span bridge has a more complex structural system composed of bridge girder, cable system, and bridge tower. Therefore it is more difficult to derive an analytical framework for lateral-torsional buckling analysis. Based on certain simplification, a nonlinear model of torsional divergence and flutter for suspension bridges was parameterized based on a single generalized coordinate (Arena & Lacarbonara, 2012). Recently, an efficient modal-based method was also developed for nonlinear aerostatic stability (Montoya, Hernández, Kareem, & Nieto, 2021). The asymmetric wind field effect on the static torsional divergence of flexible suspension bridges was studied, which shows the structural stability is worse under asymmetric wind loading (Zhang & Zhu, 2021). Different controlled (passive, semi-active dampers, TMD) and uncontrolled configurations of bridge wind-induced stability were also analyzed by FEM (Domaneschi & Martinelli, 2014; Domaneschi, Martinelli, & Po, 2015). Nevertheless, when multi-sources nonlinearity are included in the lateral-torsional buckling, FEM is still the most convenient tool for the complex structural system, such as long-span bridges.

Most existing FEM studies based on the Newton-Raphson method about static wind caused lateral-torsional buckling focus on the first critical wind speeds, where the total structural stiffness becomes zero. This approach cannot continue to track the structural equilibrium path post-buckling. However, due to the complexity of the long-span bridge, the bridge deck motion will change the AOA, which will affect the wind-caused loads and deck motion reversely. Thus, there exist three coupled nonlinearity, including geometry, aerodynamics, and material strength. Therefore there are potentially one or multiple stable states after the initial buckling because of strong nonlinearity. Table 1 lists five selected super long-span suspension bridges and associated aerostatic critical wind speeds. It clearly shows that bridge resistance capacity against static wind loads decreases rapidly when bridge span increases. Because of the

Table 1. Selected long-span suspension bridges with different span and critical aerostatic wind speeds.

Bridge Name	Span Length (m)	Aerostatic critical wind speed (m/s)
Xihoumen Bridge	1650	95
Lingding Ocean Bridge	1666	99.2
NanSha Bridge	1688	82
Lianhuashan Bridge	2100	87.5
Shiziyang Bridge	2180	85

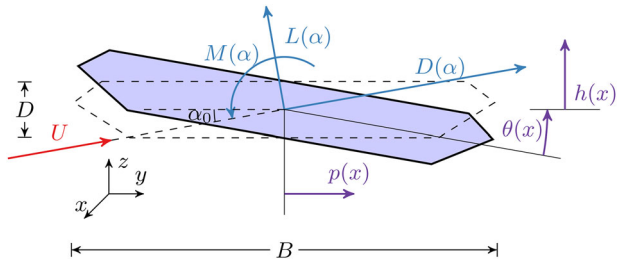


Figure 1. Wind loads axis and bridge motion axis on bridge section.

differences on geometry of bridge deck section, the relationship between span length and aerostatic critical wind speed is not straightforward. It still gives an evidence that aerostatic instability limits the capacity for spanning. Currently, the aerostatic critical wind speeds for bridge with span around 2000 m are just slightly above 80 m/s, and is very close to the bridge design wind speeds. Thus, aerostatic instability also limit the development of bridge span for future bridge construction.

Therefore, it is necessary to explore the extended wind static loads resistance even after the initial buckling. An accuracy calculative method is important to evaluate post-buckling, because the total potential of wind static loads resistance could not be found by wind tunnel test easily.

Several previous analytical studies prove the possibility of multiple stability based on simplifying assumptions on kinematics and elasticity, which cannot fully present the long-span bridge complex structural response under extreme wind loads. In the first part of this study, the multiple stability of long-span bridges under static wind loads is studied based on the arc-length method (Riks, 1979) employing different aerostatic coefficients configurations. Furthermore, turbulence-induced random vibration may also disturb the long-span bridge structure from one stable state to another if the wind speed is close to buckling critical speeds.

2. Methodology

2.1. Aerostatic stability of long-span bridge

The wind loads per unit span applied on the bridge section can be decomposed into three components along the wind axis: drag force F_D , lift force F_L and pitch moment F_M , which are caused by wind speed U with an initial angle of attack (AoA) α_0 . The bridge motion is also decomposed into motion axis with three components: sway $p(x)$, hover $p(x)$ and pitch $\theta(x)$. The two axes systems are illustrated in Figure 1.

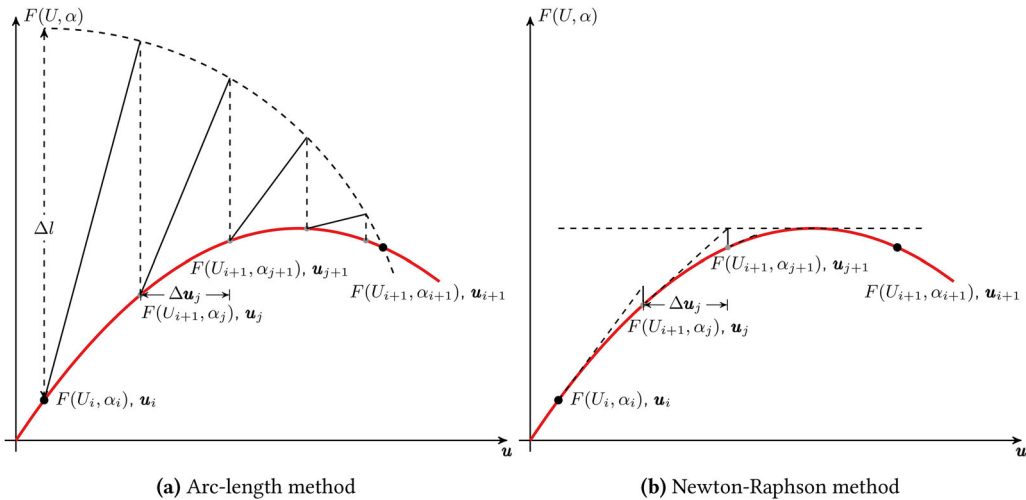


Figure 2. Two algorithms about iterative steps to calculate the equilibrium displacement using arc-length method.

$$F_D = \frac{1}{2} \rho U^2 BC_D(\alpha) \quad (1a)$$

$$F_L = \frac{1}{2} \rho U^2 BC_L(\alpha) \quad (1b)$$

$$F_M = \frac{1}{2} \rho U^2 B^2 C_M(\alpha) \quad (1c)$$

where U is the mean wind speed inclined with initial angle of attack α_0 , ρ is the air density, B and D are bridge deck width and depth, respectively. The long-span bridge displacements along span are expressed along bridge global coordinates: sway $p(x)$ (horizontal), heave $h(x)$ (vertical) and pitch $\theta(x)$ (rotation). $C_D(\alpha)$, $C_L(\alpha)$ and $C_M(\alpha)$ are drag, lift and pitch coefficients, respectively, at effective AoA $\alpha = \alpha_0 + \theta$.

The relation between forces vector in wind axis and global axis is defined as:

$$\begin{Bmatrix} F_D \\ F_L \\ F_M \end{Bmatrix} = \begin{bmatrix} \cos(\alpha_0) & \sin(\alpha_0) & 0 \\ \sin(\alpha_0) & \cos(\alpha_0) & 0 \\ 0 & 0 & 1 \end{bmatrix} \begin{Bmatrix} F_X \\ F_Y \\ F_M \end{Bmatrix} \quad (2)$$

For simplicity, the force vector and displacement per unit span in global coordinate are defined as \mathbf{F} and \mathbf{d} , respectively. Then, the constitution between wind loads and structural displacements can be defined as (Boonyapinyo et al., 2006):

$$\mathbf{F}(U, \alpha) = \mathbf{K}(\mathbf{u})\mathbf{u} = [\mathbf{K}_e + \mathbf{K}_m(\mathbf{u}) + \mathbf{K}_g^{G+W}(\mathbf{u})]\mathbf{u} \quad (3)$$

in which \mathbf{K} is the effective stiffness, \mathbf{K}_e is the conventional elastic stiffness, \mathbf{K}_m is the stiffness reduction due to material plasticity and \mathbf{K}_g^{G+W} is the nonlinear geometric stiffness caused by gravity (G) and wind loads (W). For each different wind speed U , the wind loads \mathbf{F} and structural restoring force $\mathbf{K}(\mathbf{u})\mathbf{u}$ will be affected by each other iteratively, thus the iteration methods will be used to find the equilibrium point \mathbf{u} .

2.2. Material yielding criteria

The plasticity of cable, hanger, and girder will be considered in this study. The material of cable and hanger is high-tensile steel wire, and the girder is made of constructional steel. The stiffness reduction \mathbf{K}_m will be calculated as (Boonyapinyo et al., 2006):

$$\mathbf{K}_m = -\mathbf{K}_{eg} \mathbf{G} \left(\mathbf{G}^T \mathbf{K}_{eg} \mathbf{G} \right)^{-1} \mathbf{G}^T \mathbf{K}_{eg} \quad (4)$$

where \mathbf{K}_{eg} is the effective stiffness $\mathbf{K}_{eg} = \mathbf{K}_e + \mathbf{K}_g^{G+W}(\mathbf{u})$, and \mathbf{G} is the gradient matrix of the yield surface given by Equation (5).

$$\phi = \sqrt{\left(\frac{M_x}{M_{px}}\right)^2 + \left(\frac{M_y}{M_{py}}\right)^2 + \left(\frac{M_z}{M_{pz}}\right)^2 + \left(\frac{F_x}{F_{px}}\right)^n} - 1 \quad (5)$$

where M_x , M_y and M_z are internal bending moments and torque, and F_x is the axial force. Correspondingly, M_{px} , M_{py} and M_{pz} are yielding bending moments and torque, and F_{px} is the yielding axial force. n is the exponent coefficient taken as 1.6 (Boonyapinyo et al., 2006).

2.3. Nonlinear stability searching algorithm based on arc-length methods

For the long-span bridge, aerostatic stability analysis, gravity loads, including dead loads and cable pre-tension, are normally applied first. Next, the critical wind speeds of aerostatic insatiability caused by displacement-dependent wind loads are calculated by the iterative approach composed of two layers. The outer layer is adaptive wind speeds increment sequence U_i , $i = 1, 2, 3, \dots$. For each given wind speed U_i , another iteration at the inner layer is performed to calculate the equilibrium displacement \mathbf{u}_i based on the displacement from the previous step \mathbf{u}_{i-1} .

At each inner layer iteration, there are two steps to compute the equilibrium displacement. At the first step, the initial displacement under U_i is calculated using the linearized increment procedure. In the second step, the unbalanced wind loads because of nonlinearity and additional

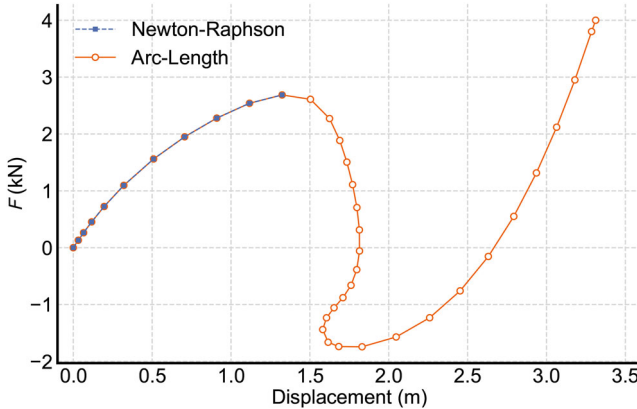


Figure 3. Equilibrium paths of hinges supported arch shell.

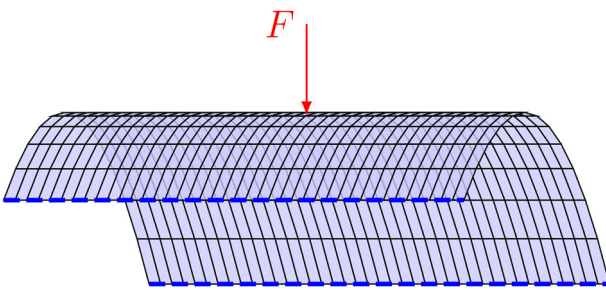


Figure 4. Finite element model of arch shell (Blue dash line means hinge support).

displacement are analyzed using the arc-length methods. The structural equilibrium equation caused by the unbalanced wind loads for j -th step using linearized incremental principle is written as:

$$[K_e + K_m(u_j) + K_g^{G+W}(u_j)]\Delta u_j = \mathbf{F}(U_i, \alpha_{j+1}) - \mathbf{F}(U_i, \alpha_j) \quad (6)$$

The arc-length method has been widely applied for structural stability problems under consideration exhibits one or more critical points. The basic concept of the arc-length method is illustrated in Figure 2a, which searches along a fixed radius arc until the intersection with equilibrium path, and more details can be found in Riks (1979). This method can search the post-buckling path after the critical points. In contrast, the traditional Newton-Raphson method, shown in Figure 2b, cannot search beyond the initial critical points because of the singularity approaching the critical points.

Figure 3 plots the equilibrium paths from two methods about an arch shell supported by hinges at two ends. The length of this arch shell is 0.25 m, and the arc length is 12° with a radius of 1 m, and the thickness of the shell is 7 mm. The arch shell is meshed as 12 (along arch side) × 40 (along straight side) with a concentrated force applied at the center of arch shell, which is also shown in Figure 4. Two dashed lines of cylinder shell in Figure 4 are hinged edges. The elastic modulus is 1.1E10Pa and Poisson ratio is 0.3. Cylinder shell is simulated by Shell 181 in ANSYS. The maximum

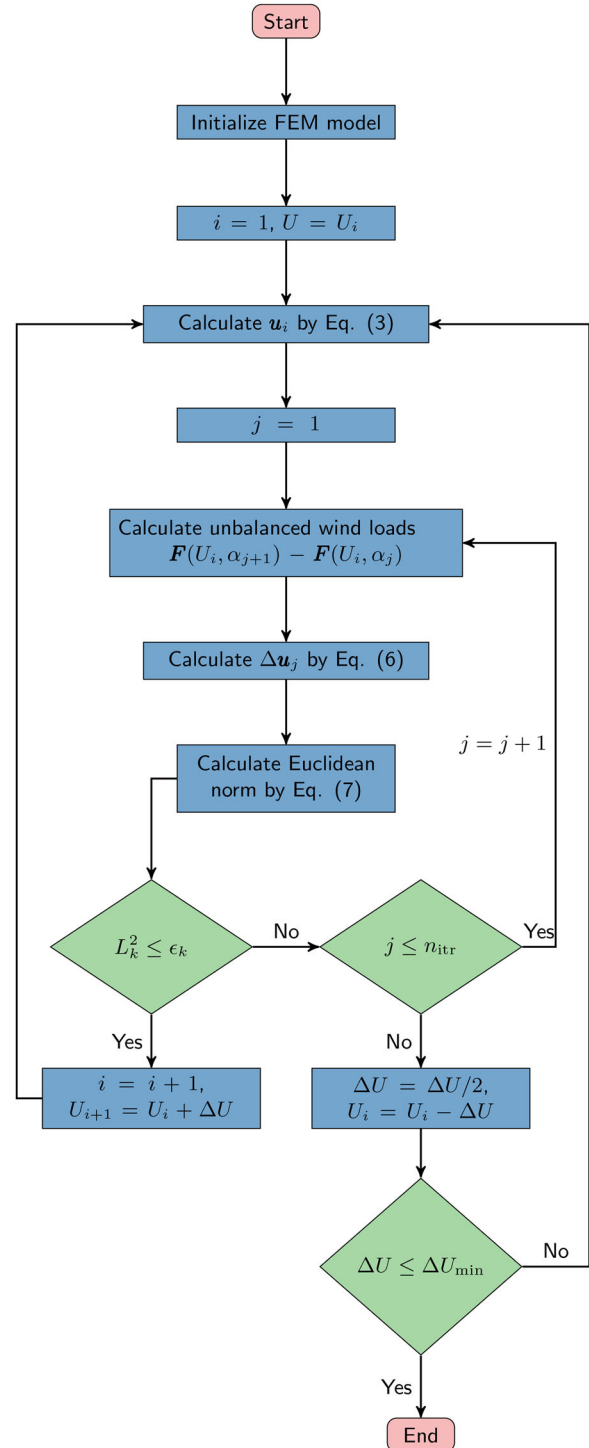


Figure 5. Flowchart of critical wind speeds searching algorithm.

force F is 4 kN, the force increment ΔF is 0.01 kN. The Newton-Raphson method can only plot the path until the first critical point at $F=2.8$ kN, while the arc-length method can track the whole equilibrium path from compressed arch to tensioned arch (post-buckling hardening). When the displacement reaches 1.8 m, the vertical load F becomes from compression to tension, while displacement is larger than 2.7 m, F converts from tension to compression again.

In the inner layer iteration, the convergence is determined by the normalized Euclidean norm of static

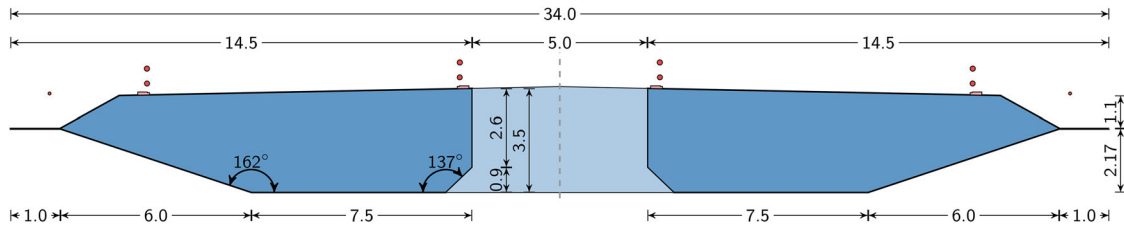


Figure 6. Geometries of Xihoumen Bridge section (Unit: m).



Figure 7. Wind tunnel test of sectional bridge model.

aerodynamic coefficients, which is equivalent to unbalance wind loads, in three directions is less than the prescribed tolerance:

$$L_k^2 = \sqrt{\frac{\sum_{N_a} [C_k(\alpha_{j+1}) - C_k(\alpha_j)]^2}{\sum_{N_a} [C_k(\alpha_j)]^2}} \leq \epsilon_k, k = D, L, M \quad (7)$$

If the wind-induced static deformation is converged for wind speed U_i , the structural stability analysis will be performed for the following wind speeds U_{i+1} increased by ΔU . When convergence criteria are not satisfied, the unbalanced wind loads will be applied to the structure in the next inner iteration until convergence criteria are satisfied or iteration reaches the maximum number n_{itr} . When $j > n_{itr}$, structural static deformation cannot converge at current wind speed, then the wind speed increment will be reduced to its half value $\Delta U = \Delta U/2$ and rerun this outer iteration. The stability analysis will be terminated when ΔU is smaller than a prescribed minimum speed ΔU_{min} . A flow chart for the long-span bridge aerostatic analysis is plotted in Figure 5.

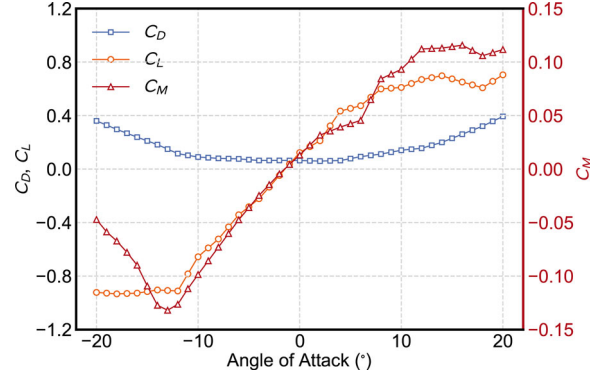


Figure 8. Aerostatic coefficients of Xihoumen Bridge.

3. Prototype of the long-span bridge

3.1. Bridge description

The prototype employed in this study is the Xihoumen Bridge. This bridge is a suspension bridge linking Jintang and Cezi islands off the East China Sea coast. It has a total length of 2713 m with a main span L as 1650 m, and east and west side spans are 578 m and 485 m, respectively. The bridge girder is 36 m wide with four traffic lanes, and the bridge deck has a clearance height approximately 72 m above water level. Due to space limitations, more information of Xihoumen bridge could be found in Song and Wang (2009) and Ma, Cui, Zhao, Yang, and Ge (2022).

The deck of Xihoumen bridge is a typical center-slotted twin-box girder with an overall width of 36.0 m and height of 3.5 m. The central slot width is 5.0 m. The detailed geometries of the bridge section are depicted in Figure 6. Based on the section shape geometries, the sectional model, shown in Figure 7, was tested in the wind tunnel to measure the aerostatic coefficients. The measured drag coefficient C_D , lift coefficient C_L and pitch coefficient C_M for the AoA α in the range $(-20^\circ, 20^\circ)$ are plotted in Figure 8.

3.2. Fem model construction

The finite element analysis is carried out on the ANSYS platform, and Figure 9 shows the whole FEM model built with various elements. Three-dimensional Euler beam elements (BEAM188) with axial stiffness are used to model the bridge towers (black line in Figure 9) with rigid lateral arms. Tensile link (LINK180) elements are employed to model the suspended cables (blue line in Figure 9) and

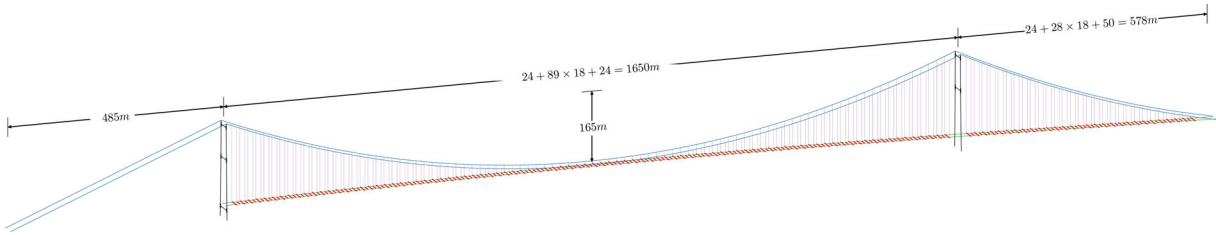


Figure 9. FEM model of Xihoumen Bridge.

Table 2. Selected structural dynamic model characteristics of Xihoumen Bridge.

No.	Modal frequency (Hz)	Modal shape*	Equivalent Mass (kg/m or kg · m ² /m)
1	0.048	SL	24702
2	0.079	ASV	47277
3	0.101	SV	28060
4	0.113	ASL	58441
5	0.254	ST	3568790
6	0.258	AST	3876440

*S: symmetric, AS: anti-symmetric, L: lateral, V: vertical, T: torsional

hangers (purple line in Figure 9). The main bridge girder (green line in Figure 9) is also modeled using Euler beam elements (BEAM188) and connected to hangers through a rigid “fish-bone” framework (Ko, Xue, & Xu, 1998).

As the bridge has two-box section, there are two “bones” connected by a rigid beam (red line in Figure 9). The bridge girders and suspension cables are discretized at the hanger locations. The towers are discretized at the elevations of bridge girders and horizontal connectors. The bases of bridge towers are considered fixed ends, and the two free ends of bridge girders are vertically supported. Additionally, the bridge girders and towers are connected through a longitudinal axis with vertical restrictions. Equivalent initial strain is applied to suspension cables and hangers as the pretension in link elements. The geometry nonlinearity and material nonlinearity have been considered, and the arc-length method is employed to calculate the structural deformation under wind loads for various wind speeds.

3.3. Structural model analysis

The typical eigenvalue analysis is performed to find the structural dynamic model properties. Table 2 shows the model characteristics selected of selected modes: first two orders for each deformation direction. The dynamic properties will be used in later turbulence-induced vibration analysis.

4. Aerostatic multi-stability of long-span bridges

According to the computation procedure in Figure 5 and the long-span bridge properties described in the previous section, the aerostatic buckling analysis can be performed for prescribed initial wind angel of attack. Figure 10 shows the bridge aerostatic displacements at middle span $x = L/2$ along horizontal p , vertical h and torsional θ directions for various wind speeds U with initial angel of attack $\alpha_0 = 3^\circ$. The displacement curves show that aerostatic buckling for

$\alpha_0 = 3^\circ$ is a typical limit-point buckling (Leahu-Aluas & Abed-Meraim, 2011). When wind speed $U \geq 103$ m/s, the structural deformation at all three direction grows dramatically, and the FEM model cannot converge to stable equilibrium point. Beside the arc-length method demonstrated in Figure 2a, the traditional Newton-Raphson (N-R) method (Deuflhard, 2011) is also employed to compare the buckling curves results. The buckling curves from two methods are identical, which proves the accuracy of nonlinear analysis methods used in this study.

When the wind initial angel of attack is $\alpha_0 = -3^\circ$, the heaving and pitching deformation increase towards different direction comparing with $\alpha_0 = 3^\circ$. At the beginning state for $U < 100$ m/s, the bridge’s aerostatic deformation at three directions increases very slowly. When $U \geq 100$ m/s, the structural deformations develop dramatically, and after $U = 130$ m/s, N-R methods cannot converge at stable equilibrium points, at which the long-span bridge divergence occurs from the point of view of traditional aerostatic analysis. However, the arc-length method can still search the next equilibrium state after a snap-through, which is shown as state 2 in Figure 11. When wind speed is in the range between 140–142 m/s, another equilibrium state emerges (state 3) in parallel with state 2. After 142 m/s, the structure enters the final divergence state (state 4), in which the deformation varies dramatically and rotational deformation changes from negative to positive.

The difference between the aerostatic displacement with different AoA are caused by the unsymmetrical C_M in Figure 8. C_M has a turning-back point when AoA is negative, while C_M roughly keeps as constant for large positive AoA. Because of the “turning-back” point, for $\alpha_0 = -3^\circ$, the torque applied on the bridge for increasing wind speeds decreases oppositely, which causes the multiple stable state shown in Figure 11.

The internal force in hangers and suspension cables is another way to examine the buckling progress (Cheng et al., 2002b). There are 10 cable segments and 10 hangers at the left span of Xihoumen Bridge are selected, and they are plotted as the thick line and numbered as shown in Figure 12.

Figure 13 plots both the hangers’ internal axis forces normalized with its initial internal force without wind force at both forward and backward sides when initial AoA $\alpha_0 = 3^\circ$. The initial normalized internal force for $U = 0$ is 1 for each hanger. As the wind speed increase, the internal force generally decreases because of growing lift forces. The internal forces in hangers located at the middle span decreased a little faster than the hangers nearby the bridge tower because

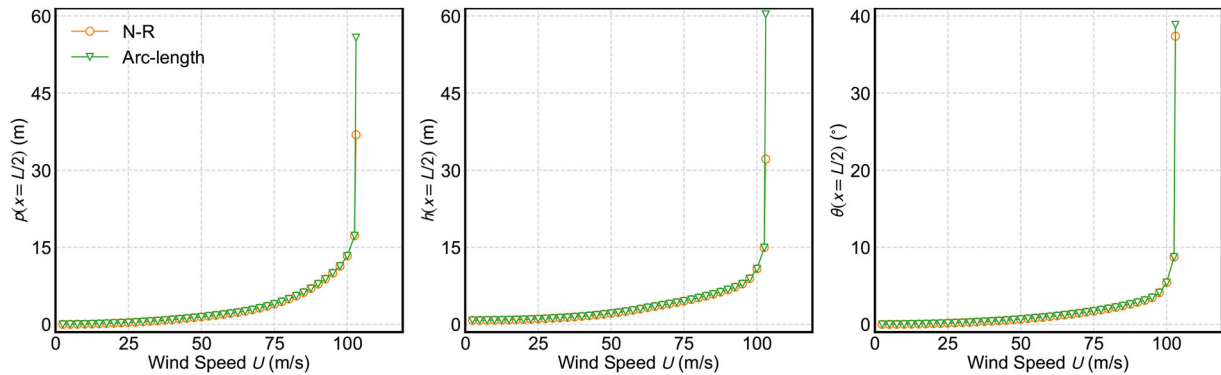


Figure 10. Aerostatic displacement for various wind speeds when initial AoA $\alpha_0 = 3^\circ$.

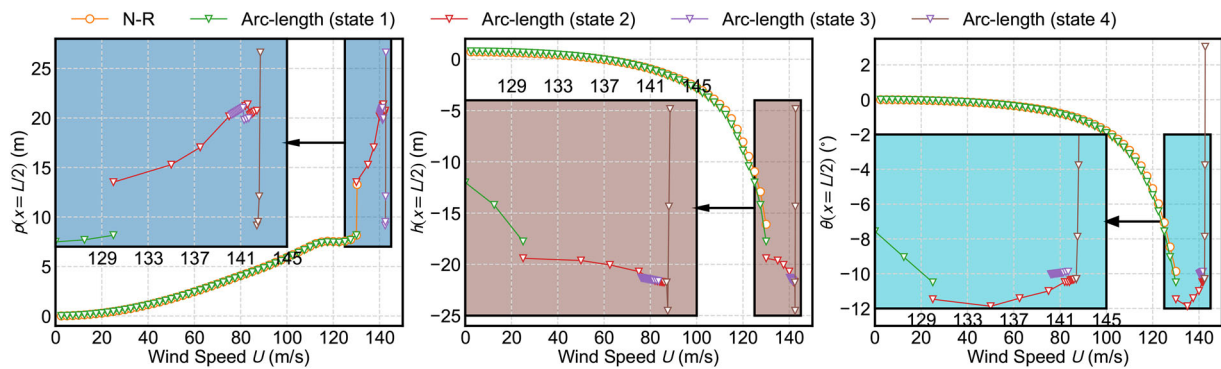
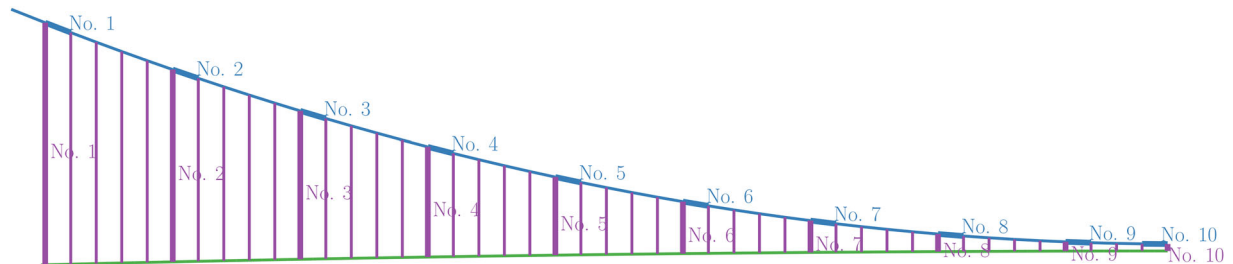


Figure 11. Aerostatic displacement for various wind speeds when initial AoA $\alpha_0 = -3^\circ$.



the bridge deck has more considerable deformation at the middle span. When wind speed approaches the critical instability value, most internal forces in the hanger drop rapidly due to large upward vertical deformations caused by aerodynamic lift.

The cable force when initial AoA $\alpha_0 = 3^\circ$ is shown in Figure 14 along the bridge span. The cable's internal forces change more uniformly as the wind speed increase. The difference between forward and backward sides is insignificant. Similar to hanger force, the cable force also drops rapidly when wind speed is close to the critical speed.

Figure 15 plots the hanger internal forces for various wind speeds when initial AoA $\alpha_0 = -3^\circ$. The hanger's internal forces vary oppositely, comparing with $\alpha_0 = 3^\circ$. Except for the No. 1 hanger, the internal force in other hangers increases due to negative lift force (push force). After the first critical point ($U=130$ m/s), the hangers' internal force increases rapidly and keeps steady for the stability state 2 corresponding to the bridge deck deformation

in Figure 11. The internal force for stability state 3 is not plotted in Figure 15 since it is very close to state 2. The hanger's force drops rapidly when the structure enters into the instability state (state 4) since the deck converts its rotation direction. The internal force in the suspension cable is shown in Figure 16. The cable force in cables at different locations is more uniform than hangers.

However, the cable on the wind forward side has a larger internal force than the backward side since the bridge deck rotates in the clockwise direction. After the bridge enters the instability state, the cable force also drops significantly as hanger forces. To further investigate the aerostatic multi-stability of suspension bridge, Figure 17 plots the bridge girder 3-directional deformed shapes along span direction for bridge aerostatic equilibrium state when wind speeds U are 143.3 and 143.9 m/s, respectively. In Figure 17, there are two equilibrium states for each U .

The overall displacement shapes along the span are not uniform for the above four equilibrium states, which is

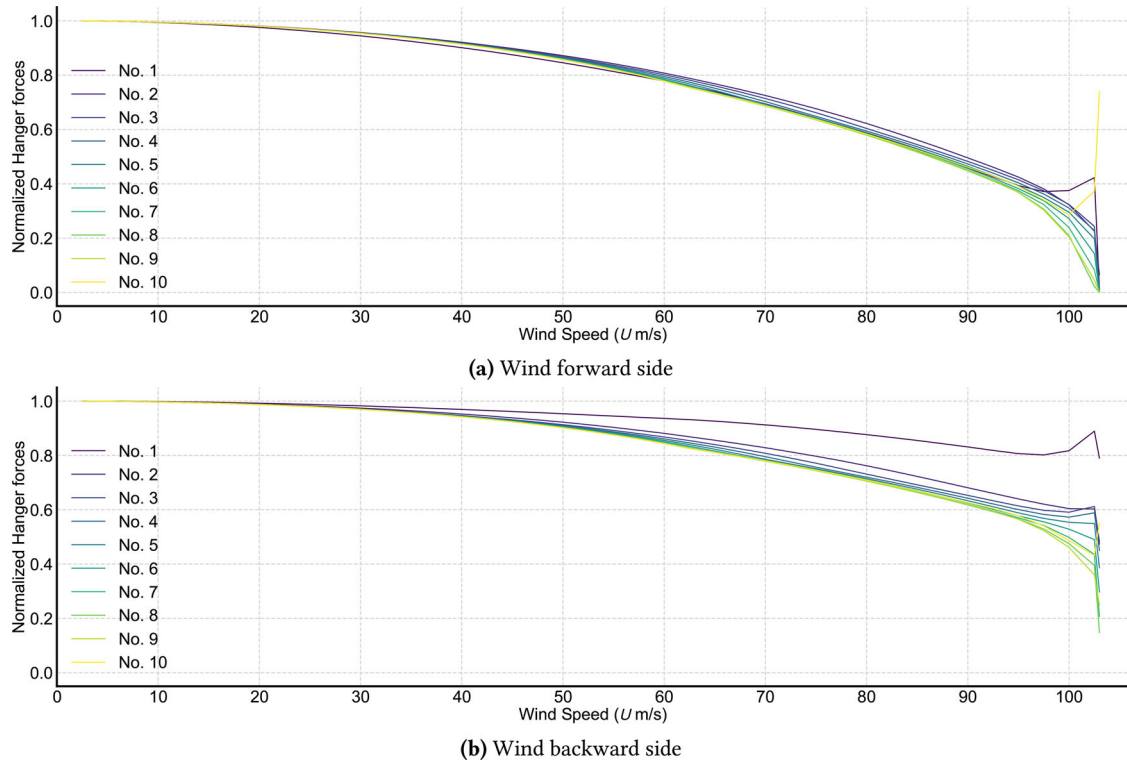


Figure 13. Internal force in hangers due to aerostatic wind loads for various wind speeds when initial AoA $\alpha_0 = 3^\circ$.

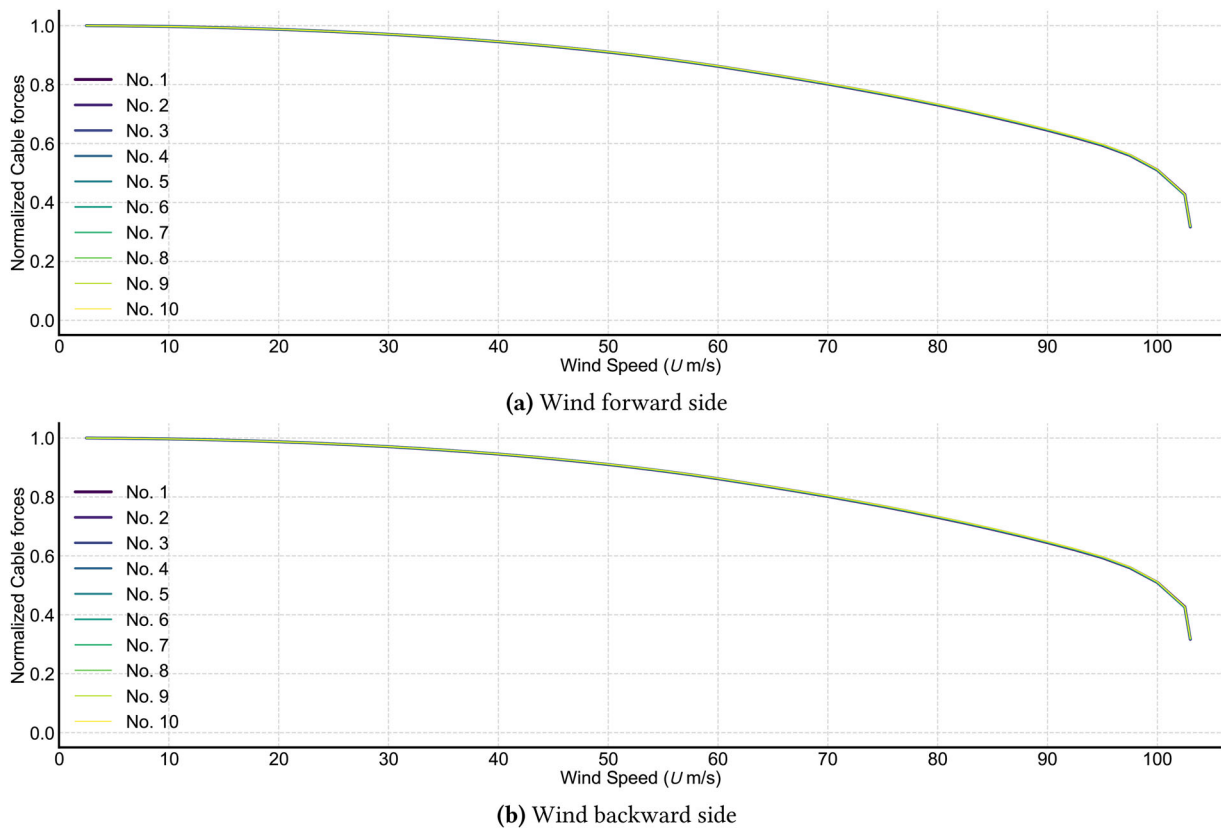


Figure 14. Internal force in suspension cable due to aerostatic wind loads for various wind speeds when initial AoA $\alpha_0 = 3^\circ$.

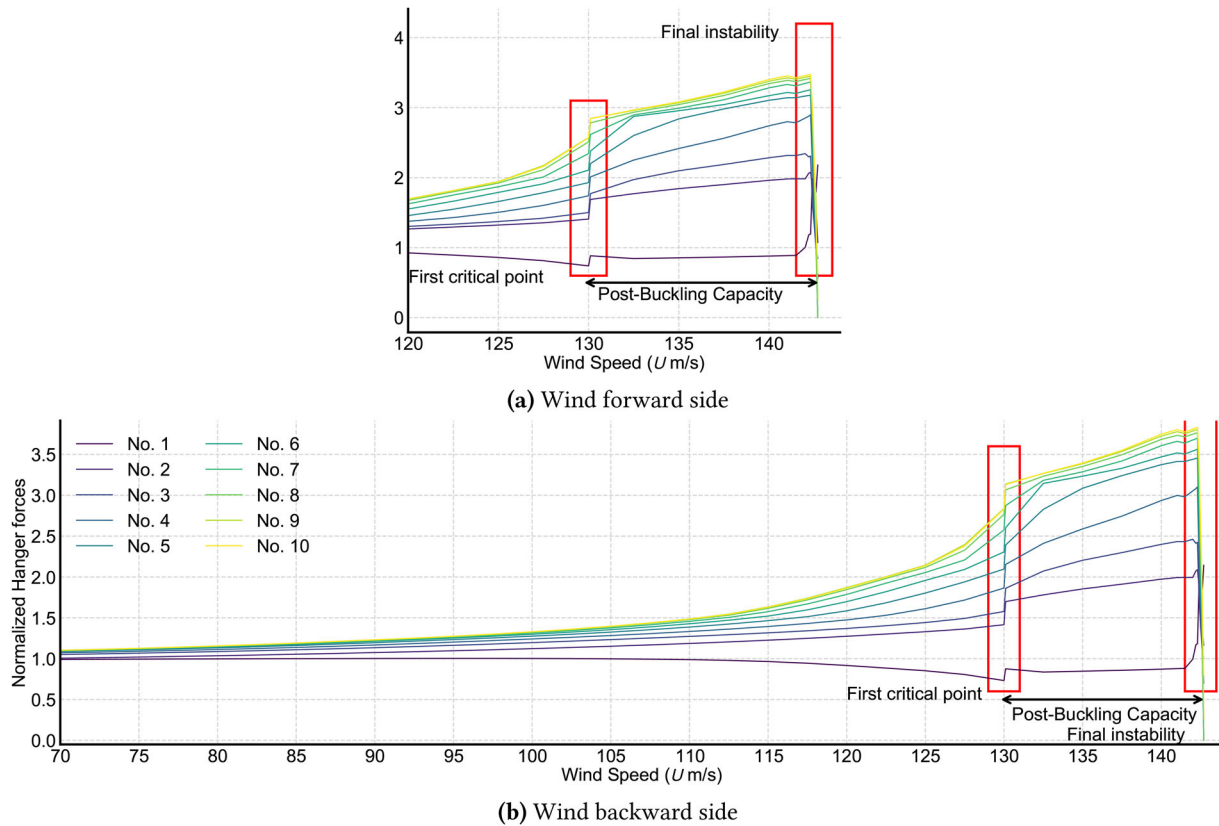


Figure 15. Internal force in hangers due to aerostatic wind loads for various wind speeds when initial AoA $\alpha_0 = -3^\circ$.

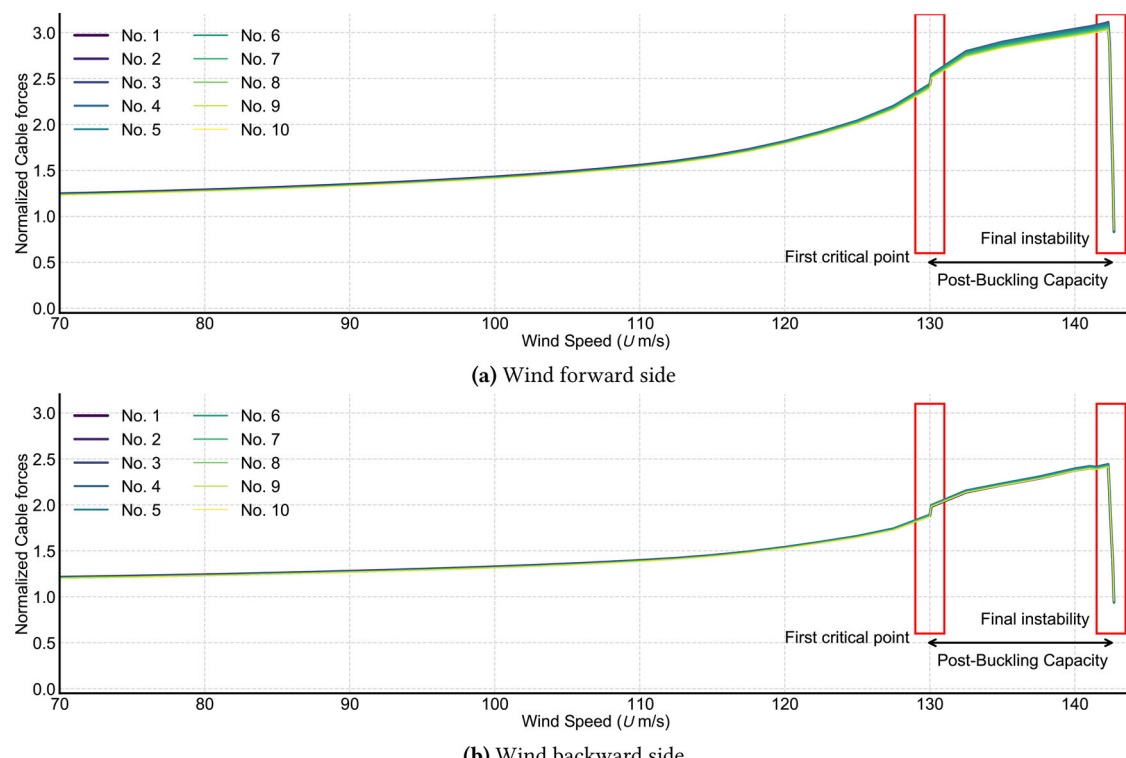


Figure 16. Internal force in suspension cable due to aerostatic wind loads for various wind speeds when initial AoA $\alpha_0 = -3^\circ$.

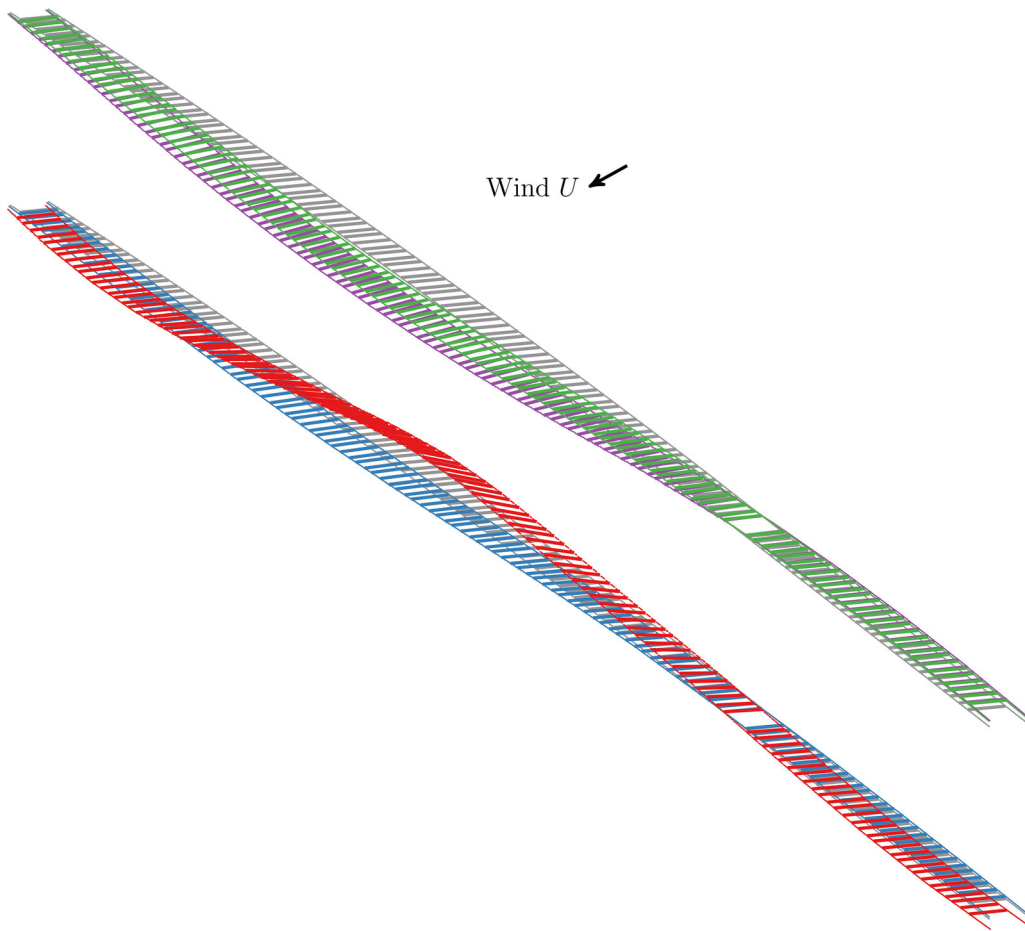


Figure 17. Deformed bridge girder under four different wind speeds with AoA as $\alpha_0 = -3^\circ$ (—: undeformed, ——: equilibrium state 1 on 143.3 m/s, ——: equilibrium state 2 on 143.3 m/s, ——: equilibrium state 1 on 143.9 m/s, ——: equilibrium state 2 on 143.9 m/s).

another evidence that aerostatic multi-stability exists for the long-span suspension bridge. Figure 18 explicitly plots the bridge girder sway, hover and pitch deformation for the above four equilibrium state.

4.1. Multi-stability of long-span bridge with modified pitch moment coefficient

The large difference in buckling curves for the initial AoA $\alpha_0 = 3^\circ$ and $\alpha_0 = -3^\circ$ is possible due to the different pitch moment curves for positive and negative angles of attack. Figure 8 shows that for negative direction pitch moment coefficient C_M begin to decrease when α exceed -12° . Correspondingly, for the AoA $\alpha_0 = -3^\circ$, the bridge rotation also start to decrease when α reaches -12° . In other words, the bridge enters into the second equilibrium state (state 2), as shown in Figure 11. In contrast, the pitch moment coefficient C_M remains stable for positive direction, and the bridge directly enters the instability state without the second equilibrium state.

In light of this difference, this study examines the buckling curve for a modified C_M curve, as shown in Figure 19. The modified curve has a “increase-then-decrease” shape in positive α region similar to negative region α . The arc-length-based aerostatic buckling analysis when the initial AoA $\alpha_0 = 3^\circ$ is performed with the modified pitch moment curve and the buckling curve is plotted in Figure 20. Similar

to the original C_M curve with $\alpha_0 = -3^\circ$, the buckling curve for modified C_M with $\alpha_0 = 3^\circ$ can be extended by arc-length methods when the N-R method cannot converge when $U = 101$ m/s. After the initial buckling (state 1), the buckling curve diverges into two different equilibrium states (state 2 and state 3). The aerostatic rotation of State 2 is around 4° , and the rotation for State 3 is around 16° , which is also the turning point for the modified C_M curve.

Similarly, the bridge pitch deformation along span is plotted in Figure 21 for five equilibrium states when the wind speeds in a small range from 101 to 104 m/s. However, the pitch deformation changes back and forth corresponding to state 2 and state 3 in Figure 20. The hangers’ internal forces are also plotted in Figure 22. Before $U = 104$ m/s, their internal forces decrease gradually similar to Figure 13. However, after $U = 104$ m/s their internal forces start to fluctuate up and down corresponding to the changes between equilibrium states.

5. Long-span bridge buckling affected by turbulence induced vibration

In the natural wind field, the additional turbulence and turbulence-induced vibration cannot be ignored in structural stability analysis (Zhang et al., 2010). In regular turbulence induce buffeting analysis, the linear assumption is applied

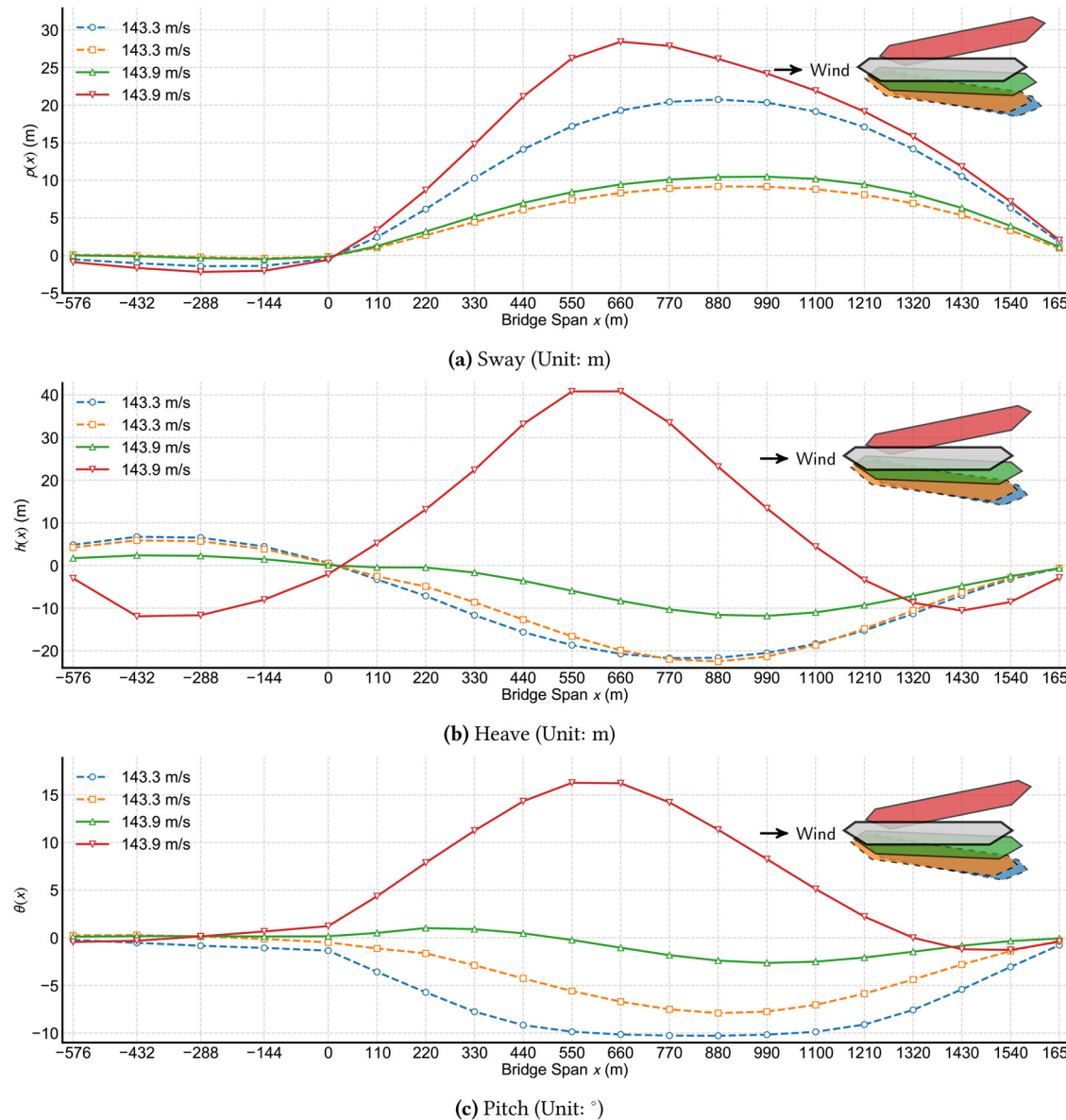


Figure 18. Bridge girder 3 directional displacements along span when $\alpha_0 = -3^\circ$ (The sectional motion at center span is plotted with corresponding color; dashed line means the two equilibrium states at 143.3 m/s, and solid means the two equilibrium states at 143.9 m/s).

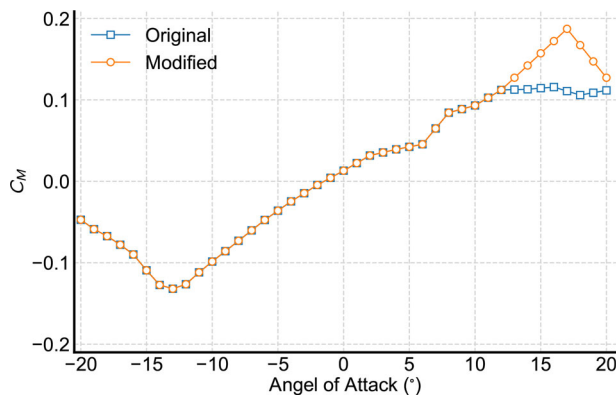
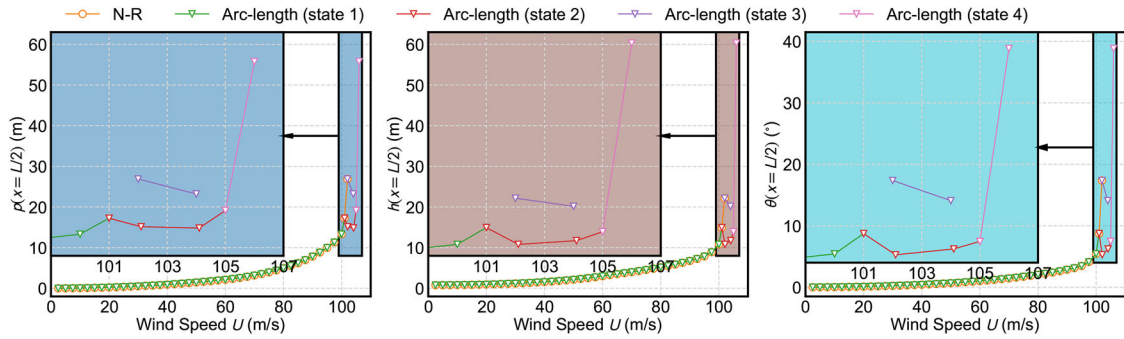
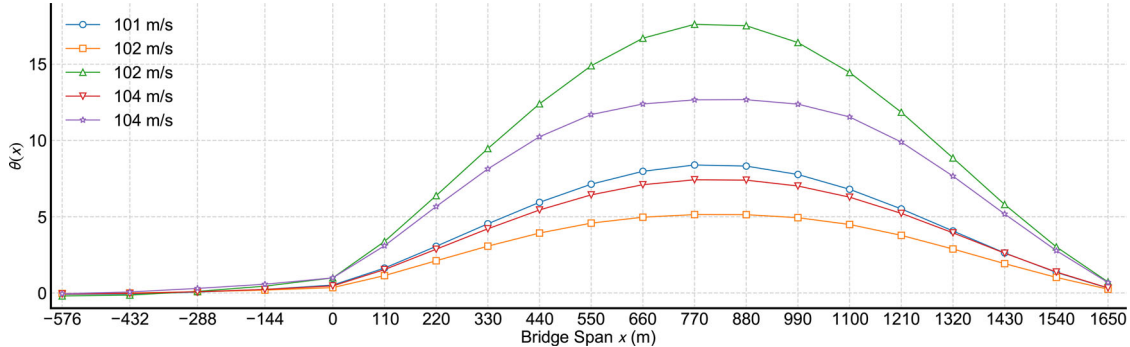
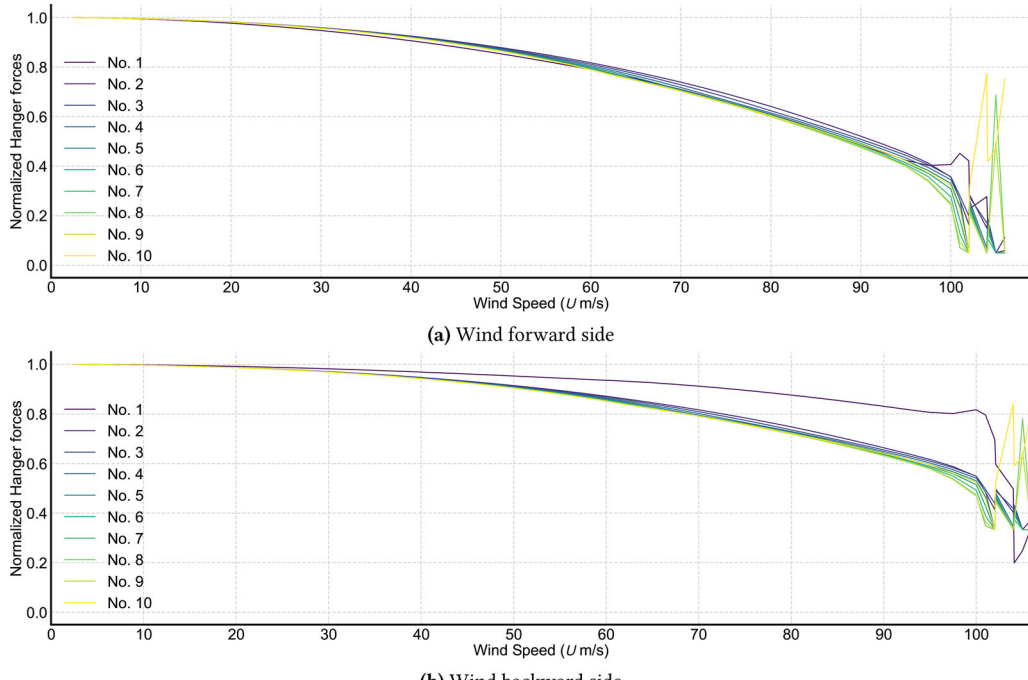


Figure 19. Modified pitch moment coefficient curve.

on both structure and aerodynamic of dynamic structural motion. However, when wind speed is close to the critical aerostatic instability value, the structural nonlinearity and motion-dependent aerodynamic force cannot be ignored for

turbulence-induced vibration. Furthermore, the excessive displacements induced by both aerostatic force and turbulence effect may cause the material plasticity of the bridge girder. Therefore, the long-span bridge may buckle at a lower wind speed. Because of the limitation of the arch-length method to dynamic calculation, Newton-Raphson method is used to calculate the dynamic response of bridge in this section. And how first critical wind speed affected by turbulence is focused in this section.

For the dynamic analysis based on FEM, the additional aeroelastic force and turbulence admittance should be considered. The fluid-structure interaction aeroelastic force can be evaluated by additional stiffness and damping matrix in ANSYS FEM platform (Hua, Chen, Ni, & Ko, 2007) and correlated multi-variate buffeting force including turbulence and aerodynamic admittance applied on bridge girder nodes (Zhao & Yaojun, 2013) are simulated by spectrum superposition method (Shinozuka, 1971).

Figure 20. Aerostatic displacement for various wind speeds when initial AoA $\alpha_0 = 3^\circ$.Figure 21. Bridge girder 3 directional displacements along span when $\alpha_0 = -3^\circ$.Figure 22. Internal force in hangers due to aerostatic wind loads for various wind speeds when initial AoA $\alpha_0 = 3^\circ$.

The flutter derivatives $H_1^* \sim H_4^*$ and $A_1^* \sim A_4^*$ used in aerostatic force are obtained from internal wind tunnel test report about Xihoumen Bridge (Ge, Xiang, & Song, 2004). Aerodynamic admittance function $\chi_{L_{bu}}$, $\chi_{L_{bw}}$, $\chi_{M_{bu}}$ and $\chi_{M_{bw}}$ are taken as Sears function (Sears, 1941). The along-wind and vertical turbulence spectra are assumed to follow von Kármán and Panofsky type, respectively, as in Equation (8). In this study, the turbulence intensity is assumed as 0.12

and 0.10 for I_u and I_w , respectively according to the Chinese bridge design code (Ministry of Transports of the People's Republic of China, 2018). The integral length L_u and L_w are considered dependent on turbulence intensity as described in Zhao, Cui, and Ge (2019).

$$\frac{nS_{uu}}{\sigma_u^2} = \frac{4f_u}{(1 + 70.78f_u^2)^{5/6}} \quad (8a)$$

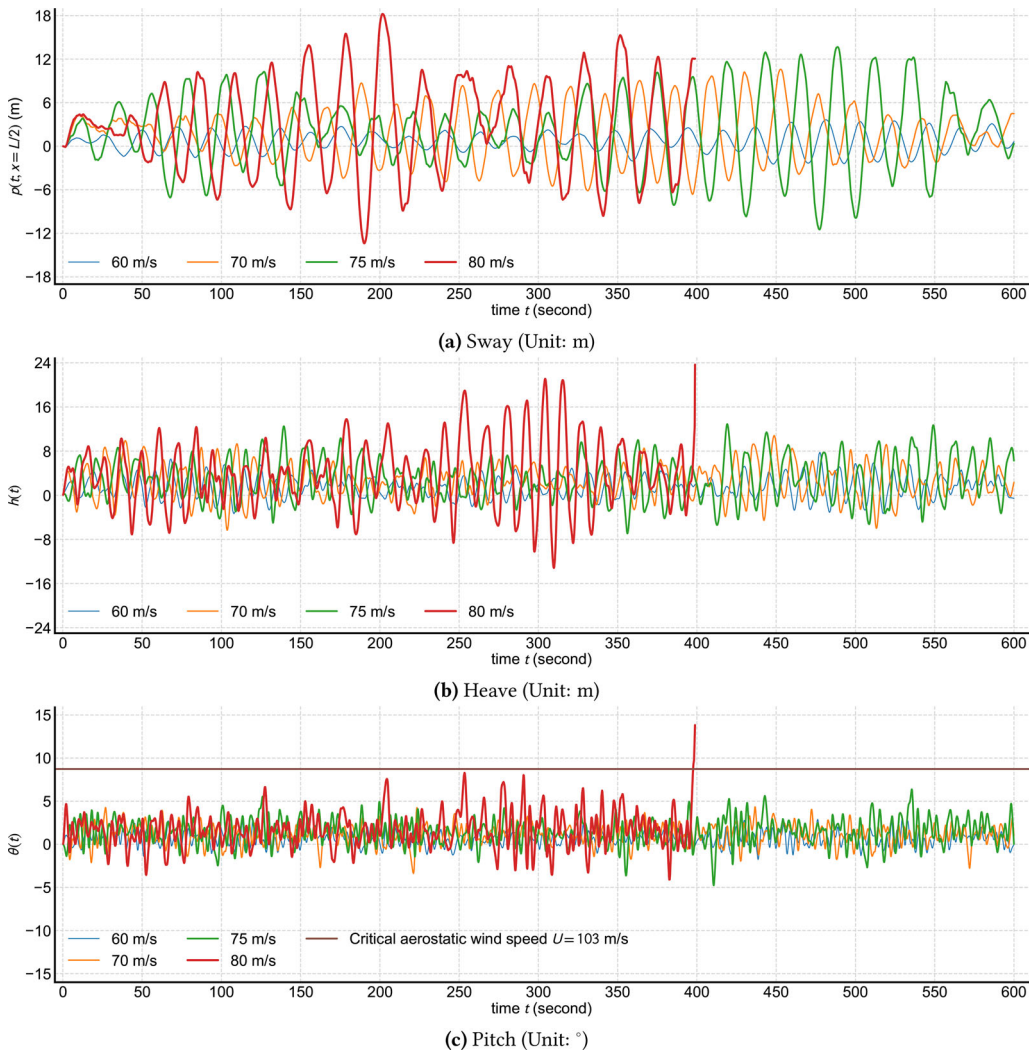


Figure 23. Bridge girder 3 directional displacements along span when $\alpha_0 = -3^\circ$.

$$\frac{nS_{ww}}{u_*^2} = \frac{3.36f_z}{1 + 10f_z^{5/3}} \quad (8b)$$

where $f_u = nL_u/U$, $f_z = nz/U$ is the reduced frequency dependent on turbulence integral length and elevation, respectively, and u_* is assumed as $u_*^2 = \sigma_u^2/6$. The definition of turbulence intensity I_u and I_w and integral length L_u and L_w can be found in Zhao et al. (2019) and Simiu and Scanlan (1996).

The span-wise correlation of buffeting forces is assumed to be the same as the turbulence correlation. Both along-wind and vertical turbulence coherence functions are expressed as Simiu and Scanlan (1996):

$$\text{coh}(x_1, x_2; \omega) = \exp\left(-\frac{c\omega|x_1 - x_2|}{2\pi U}\right) \quad (9)$$

where c is the decay coefficient and is assumed as 10, and x_1 and x_2 are the coordinates of two points of interest along the bridge span.

The turbulence defined in the frequency domain by Equations (8) and (9) can be converted to time-domain by the spectral representation method in Shinozuka (1971). Next, the chord-wise aerodynamic admittance can be applied to the digital turbulence wind field by the rational

function expressed in Chen, Matsumoto, and Kareem (2000).

$$u_i(t) = \sqrt{4\pi\Delta n} \sum_{m=1}^i \sum_{l=1}^N |H_{im}(n_{ml})| \cos(2\pi n_{ml}t - \theta_{im}(n_{ml}) + \Phi_{ml}) \quad (10)$$

According to the dynamic time history integration algorithm in Zhang et al. (2010), the long-span bridge middle span motion histories at three directions are plotted in Figure 23 for four different wind speed 60, 70, 75, and 80 m/s. As the wind speeds increase, the bridge vibration amplitudes increase dramatically because of aeroelastic effect (Zhang et al., 2010). However, when wind speed increases to 80 m/s, the bridge suddenly becomes unstable when $t \approx 400$ s. Therefore, the early buckling is possible due to jumping to the unstable region caused by large rotation. The bridge rotation angle θ increases abruptly from 0 to over 10° , after which the bridge structure cannot converge to a stable solution and becomes unstable. Comparing the critical wind speed ($U = 103$ m/s) for aerostatic structural instability, the ultimate rotation at critical wind speed in smooth wind flow is only 8.7° .

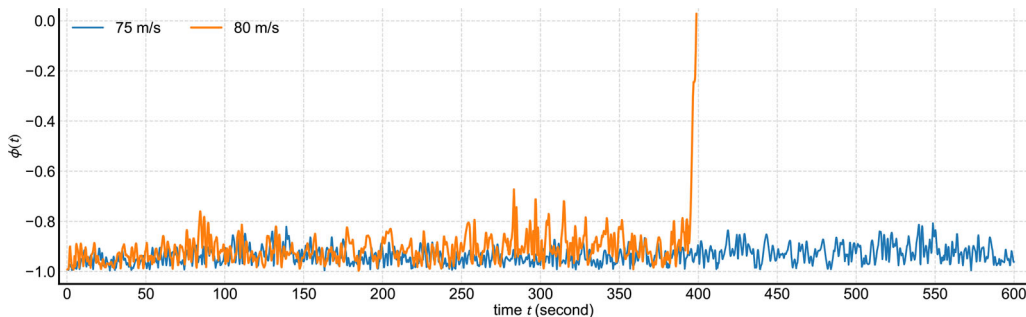


Figure 24. Element yielding surface index during buffeting when $\alpha_0 = -3^\circ$.

Figure 24 shows the yielding surface value in Equation (5) of the bridge girder element at the middle span, which clearly shows that the material yielding at the middle span is the direct reason for bridge buckling. This concludes that torsional instability of the long-span bridge can occur under the turbulent wind environment even when mean wind speeds are much lower than the critical wind speed in the smooth wind flow. For the initial AoA is $\alpha_0 = 3^\circ$, because the critical speed of aerostatic buckling is much higher than critical wind speed flutter, similar early buckling phenomenon as in Figure 24 does not happen for initial AoA is $\alpha_0 = 3^\circ$.

6. Conclusions

This study first reviews state-of-the-art methodology to calculate the aerostatic instability of long-span bridges using the finite element method, in which the structural and aerodynamic nonlinearity are evaluated through the classical Newton-Raphson method. This study proposes to use the arc-length method to track the bridge equilibrium path under the wind loads. The main findings in this study can be summarized as the following.

1. The arc-length method can still search out the second structural stable states after the first critical instability point when the aerodynamic pitch moment curve has “turning-pint” at a large angle of attack. In opposite, when the pitch moment curve increases monotonously, the bridge structure will buckle at the first critical instability point without a second equilibrium state.
2. The arc-length method also finds out that, after the first critical instability point, the long-span bridge structure may represent more than one equilibrium state for the same wind speed (multi-stability), and structural motion shape also changes largely for corresponding equilibrium states.
3. In the second part of this study, aerostatic structural stability is evaluated in the turbulent wind field. The simulation results demonstrate that long-span bridges may buckle at a lower wind speed comparing with the critical wind speeds in a smooth flow. This early buckling is caused by material yielding induced by large instantaneous deformation.

Overall, the sophisticated bridge section design with “turning-back” point on pitch coefficient C_M curve can provide extra post-buckling wind resistance and additional safety margins at significant large wind speeds.

Acknowledgments

Any opinions, findings and conclusions or recommendations are those of the authors and do not necessarily reflect the views of the above agencies.

Disclosure statement

No potential conflict of interest was reported by the authors.

Funding

The authors gratefully acknowledge the support of National Natural Science Foundation of China (52008314, 52078383).

References

- Arena, A., & Lacarbonara, W. (2012). Nonlinear parametric modeling of suspension bridges under aeroelastic forces: Torsional divergence and flutter. *Nonlinear Dynamics*, 70(4), 2487–2510. doi:[10.1007/s11071-012-0636-3](https://doi.org/10.1007/s11071-012-0636-3)
- Bisplinghoff, R. L., & Ashley, H. (2013). *Principles of aeroelasticity* (2nd ed.). North Chelmsford, MA: Courier Corporation.
- Boonyapinyo, V., Lauhatanon, Y., & Lukkunaprasit, P. (2006). Nonlinear aerostatic stability analysis of suspension bridges. *Engineering Structures*, 28(5), 793–803. doi:[10.1016/j.engstruct.2005.10.008](https://doi.org/10.1016/j.engstruct.2005.10.008)
- Boonyapinyo, V., Yamada, H., & Miyata, T. (1994). Wind-induced nonlinear lateral-torsional buckling of cable-stayed bridges. *Journal of Structural Engineering*, 120(2), 486–506. doi:[10.1061/\(ASCE\)0733-9445\(1994\)120:2\(486\)](https://doi.org/10.1061/(ASCE)0733-9445(1994)120:2(486))
- Chen, X., Matsumoto, M., & Kareem, A. (2000). Time domain flutter and buffeting response analysis of bridges. *Journal of Engineering Mechanics*, 126(1), 7–16. doi:[10.1061/\(ASCE\)0733-9399\(2000\)126:1\(7\)](https://doi.org/10.1061/(ASCE)0733-9399(2000)126:1(7))
- Cheng, J., Jiang, J.-J., Xiao, R.-C., & Xiang, H.-F. (2002a). Advanced aerostatic stability analysis of cable-stayed bridges using finite-element method. *Computers & Structures*, 80(13), 1145–1158. doi:[10.1016/S0045-7949\(02\)00079-2](https://doi.org/10.1016/S0045-7949(02)00079-2)
- Cheng, J., Jiang, J.-J., Xiao, R.-C., & Xiang, H.-F. (2002b). Nonlinear aerostatic stability analysis of jiang yin suspension bridge. *Engineering Structures*, 24(6), 773–781. doi:[10.1016/S0141-0296\(02\)00006-8](https://doi.org/10.1016/S0141-0296(02)00006-8)
- Cheng, J., Xiao, R.-C., Xiang, H.-F., & Jiang, J.-J. (2003). NASAB: A finite element software for the nonlinear aerostatic stability analysis of cable-supported bridges. *Advances in Engineering Software*, 34(5), 287–296. doi:[10.1016/S0965-9978\(03\)00010-3](https://doi.org/10.1016/S0965-9978(03)00010-3)

- Deuflhard, P. (2011). *Newton methods for nonlinear problems: Affine invariance and adaptive algorithms* (Vol. 35). Berlin: Springer Science & Business Media.
- Dimentberg, M. (1999). Nonlinear torsional divergence: Certain exact solutions. *Journal of Fluids and Structures*, 13(6), 779–784. doi:10.1006/jfls.1999.0229
- Domaneschi, M., & Martinelli, L. (2014). Refined optimal passive control of buffeting-induced wind loading of a suspension bridge. *Wind and Structures*, 18(1), 1–20. doi:10.12989/was.2014.18.1.001
- Domaneschi, M., Martinelli, L., & Po, E. (2015). Control of wind buffeting vibrations in a suspension bridge by TMD: Hybridization and robustness issues. *Computers & Structures*, 155, 3–17. doi:10.1016/j.compstruc.2015.02.031
- Dunn, P., & Dugundji, J. (1992). Nonlinear stall flutter and divergence analysis of cantilevered graphite/epoxy wings. *AIAA Journal*, 30(1), 153–162. doi:10.2514/3.10895
- Ge, Y., Xiang, H., & Song, J. (2004). *Xihoumen long-span suspension bridge aerodynamic performance and wind-induce vibration control report*. Shanghai: Tongji University.
- Hirai, A., Okauchi, I., Ito, M., & Miyata, T. (1967). Studies on the critical wind velocity for suspension bridges. In *Proceedings of the international research seminar on wind effects on buildings and structures*. Ontario, Canada: University of Toronto Press.
- Hua, X., Chen, Z., Ni, Y., & Ko, J. (2007). Flutter analysis of long-span bridges using ansys. *Wind and Structures*, 10(1), 61–82. doi:10.12989/was.2007.10.1.061
- Ko, J., Xue, S., & Xu, Y. (1998). Modal analysis of suspension bridge deck units in erection stage. *Engineering Structures*, 20(12), 1102–1112. doi:10.1016/S0141-0296(97)00207-1
- Leahu-Aluas, I., & Abed-Meraim, F. (2011). A proposed set of popular limit-point buckling benchmark problems. *Structural Engineering and Mechanics*, 38(6), 767–802. doi:10.12989/sem.2011.38.6.767
- Ma, T., Cui, W., Zhao, L., Yang, Y., & Ge, Y. (2022). Optimization of long-span suspension bridge erection procedure considering flutter risk in mixed extreme wind events. *Journal of Wind Engineering and Industrial Aerodynamics*, 222, 104889. doi:10.1016/j.jweia.2021.104889
- Ministry of Transport of the People's Republic of China. (2018). *Wind-resistant design specification for highway bridges*. (JTGT 3360-01-2018). American Society of Civil Engineers.
- Montoya, M. C., Hernández, S., Kareem, A., & Nieto, F. (2021). Efficient modal-based method for analyzing nonlinear aerostatic stability of long-span bridges. *Engineering Structures*, 244, 112556. doi:10.1016/j.engstruct.2021.112556
- Riks, E. (1979). An incremental approach to the solution of snapping and buckling problems. *International Journal of Solids and Structures*, 15(7), 529–551. doi:10.1016/0020-7683(79)90081-7
- Sears, W. R. (1941). Some aspects of non-stationary airfoil theory and its practical application. *Journal of the Aeronautical Sciences*, 8(3), 104–108. doi:10.2514/8.10655
- Shinozuka, M. (1971). Simulation of multivariate and multidimensional random processes. *The Journal of the Acoustical Society of America*, 49(1B), 357–368.
- Simiu, E., & Scanlan, R. H. (1996). *Wind effects on structures: Fundamentals and applications to design* (3rd ed.). New Jersey, USA: John Wiley & Sons.
- Simiu, E., & Yeo, D. (2019). *Wind effects on structures: Modern structural design for wind* (4th ed.). New Jersey, USA: Wiley-Blackwell.
- Song, H., & Wang, X. (2009). Zhoushan xihoumen bridge—The world's longest box girder suspension bridge. In *Iabse workshop: Recent major bridges, shanghai, china*, 11–12 May 2009.
- Yang, Y., Zhou, R., Ge, Y., Mohotti, D., & Mendis, P. (2015). Aerodynamic instability performance of twin box girders for long-span bridges. *Journal of Wind Engineering and Industrial Aerodynamics*, 145, 196–208. doi:10.1016/j.jweia.2015.06.014
- Zhang, Z., & Zhu, L. (2021). Wind-induced symmetric and asymmetric static torsional divergence of flexible suspension bridges. *Journal of Fluids and Structures*, 103, 103263. doi:10.1016/j.jfluidstructs.2021.103263
- Zhang, Z., Chen, Z., Hua, X., Li, C., & Ge, Y. J. (2010). Investigation of turbulence effects on torsional divergence of long-span bridges by using dynamic finite-element method. *Journal of Bridge Engineering*, 15(6), 639–652. doi:10.1061/(ASCE)BE.1943-5592.0000101
- Zhang, Z., Ge, Y., & Chen, Z. (2015). On the aerostatic divergence of suspension bridges: A cable-length-based criterion for the stiffness degradation. *Journal of Fluids and Structures*, 52, 118–129. doi:10.1016/j.jfluidstructs.2014.10.005
- Zhao, L., Cui, W., & Ge, Y. (2019). Measurement, modeling and simulation of wind turbulence in typhoon outer region. *Journal of Wind Engineering and Industrial Aerodynamics*, 195, 104021. doi:10.1016/j.jweia.2019.104021
- Zhao, L., & Yaojun, G. (2013). Wind induced buffeting reliability of long-span cable-stayed bridge using stochastic finite element method. *Disaster Advances*, 6(3), 32–40.